Bull. Mater. Sci., Vol. 40, No. 7, December 2017, pp. 1335–1345
https://doi.org/10.1007/s12034-017-1491-0

Chemical synthesis and characterization of nano-sized rare-earth ruthenium pyrochlore compounds $Ln_2Ru_2O_7$ (Ln = rare earth)

R A PAWAR[1,*], A K NIKUMBH[2], D S BHANGE[3], N J KARALE[2], D V NIGHOT[2] and M B KHANVILKAR[2]

[1]Department of Chemistry, PDEA's Baburaoji Gholap College, Sangvi, Pune 411 027, India
[2]Department of Chemistry, Savitribai Phule Pune University, Pune 411 007, India
[3]Department of Chemistry, Shivaji University, Kolhapur 416 004, India
*Author for correspondence (rapawar9@gmail.com)

MS received 6 November 2016; accepted 14 March 2017; published online 6 December 2017

Abstract. The rare-earth ruthenium pyrochlores $Ln_2Ru_2O_7$ (Ln = La^{3+}, Pr^{3+}, Nd^{3+}, Sm^{3+} and Gd^{3+}) have been synthesized by the tartrate co-precipitation method, which allowed control of their composition and morphology. The preparation processes were monitored by thermal studies (TG-DTA). The obtained ruthenates were characterized by X-ray diffraction (XRD), TEM, d.c. electrical conductivity, thermoelectric power and dielectric constant measurements. X-ray diffraction patterns for all pyrochlore samples indicate a single-phase crystalline material with a cubic structure except for $LaRuO_3$, which shows perovskite orthorhombic structure. The structural parameter for the solid obtained was successfully determined by Rietveld refinement based on the analysis of powder XRD pattern. The TEM photographs of these compounds exhibited the average particle size in the range of 36.4–73.8 nm. The data on the temperature variation of d.c. electrical conductivity showed that all rare-earth ruthanates are semiconductors and major carriers are electrons. The conduction mechanism of these compounds seems to be oxygen non-stoichiometry. The variation of dielectric constant at various frequencies showed initially interfacial polarization up to 275 kHz and beyond, which shows domain wall motion.

Keywords. Pyrochlore ruthenates; nano-sized; tartrate precursor; d.c. electrical conductivity; dielectric properties.

1. Introduction

Pyrochlore oxides constitute a large family of transition metal oxides with the chemical formula $A_2B_2O_7$, where A is a larger cation and B is a smaller transition metal ion. Pyrochlore ruthenates containing rare-earth elements with general formula $Ln_2Ru_2O_7$ show a wide diversity of properties. The pyrochlore ruthenates are technologically important materials as catalysts [1], electrocatalysts [2] and conducting components in thick-film resistors [3]. Their electronic properties are of intrinsic interest, since the Ru:4d electrons are on the borderline between localized and itinerant behaviour. For example, some of the rare-earth ruthenates $Ln_2Ru_2O_7$ (Ln = La−Lu) are electrical insulators and the others are all semiconductors with a spontaneous ruthenium atomic moment [4,5].

An ideal requirement of metal-ruthenate-based materials for advanced applications is the ability to synthesize nearly monodisperse, smooth, high-purity and non-agglomerated sub-micrometre-sized powders with control over chemical homogeneity, crystallinity, crystalline phase content and microstructure. The printed circuit technology requires a denser packing of features and a precise control over their performance. The catalytic activity and selectivity also vary with the size and the surface area of the particles [6]. Thus, a method to form the uniform submicrometre-sized particles also is desirable for this application.

The general formula of pyrochlore ruthanates can be written as $A_2B_2O_6O'$, with Ru on the B site, and they have an ordered superstructure of fluorite with a cubic lattice parameter of about 1.0 nm, roughly twice that of fluorite structure. The A, B, O and O′ ions occupy four crystallographic sites 16*c*, 16*d*, 48*f* and 8*b*, respectively. The sites 8*b* and 48*f* are occupied by oxygen ions, which deviate from the centre of tetrahedron from two A and two B ions. The $A_2B_2O_6O'$ structure has distorted BO_6 octahedra that share corners to form a tetrahedral lattice of the formula B_2O_6 [7]. The A cations are present at the centre of the hexagonal rings of oxygens (formed from six BO_6 octahedra) with two more oxygens (O′) located above and below the ring and hence they are eight-coordinated. Each O′ atom is tetrahedrally coordinated with A cations, and the A and O′ atoms form a tetrahedral lattice of the formula A_2O'. The B_2O_6 and A_2O' lattices interpenetrate, and the B and A cations interact through B–O–A linkages. Each O is surrounded with two B and two A cations in a distorted tetrahedron (local C_2v symmetry). The pyrochlore $A_2B_2O_6O'$ tolerates a high degree of vacancy on the O′ anion sites; hence, its composition is $A_2B_2O_6(O')_{1-y}$ i.e., $A_2B_2O_{7-y}$ if the distinction between O and O′ is not made [7].

The phase transition could be achieved either by increasing temperature or by changing composition [8–11]. The beauty of the pyrochlore system lies in its ability to incorporate an incredibly diverse range of elements, usually by combining 2+/5+ and 3+/4+ cations on the A and B sites, respectively, in proportions such that the average ionic radius ratio of cation sites (r_A/r_B) lies within the pyrochlore stability field. Subramanian *et al* [8] reported that pyrochlore structures are formed when ratio r_A/r_B lies between 1.46 and 1.78. Defect fluorite structures are produced when r_A/r_B falls below this range, whilst at higher values, the stable structure is monoclinic.

Existing methods to prepare metal ruthenates generally involve solid-state reactions of ruthenium metal or ruthenium dioxide and the corresponding metal carbonates or oxides at high temperature in air or oxygen atmosphere with subsequent milling of the products to reduce the particle size [12,13]. These approaches, however, do not allow good control over purity, size, composition, crystallinity and morphology in the micrometre- and submicrometre-sized particles. Hydrothermal techniques have been widely applied to the synthesis of $Ln_2Ru_2O_7$ under subcritical hydrothermal conditions [14].

Liquid-phase routes also have been used to form rare-earth ruthenate powders. Sol–gel, soft chemistry and spray-pyrolysis routes have been used for the synthesis of these oxides [15,16]. In this paper, we have reported on the metal tartrate precursor method for preparation of nano-sized rare-earth ruthenium pyrochlores. This method of powder preparation provides a viable alternative to solid-state reactions, allowing a better control of stoichiometry, purity, size, crystallinity and morphology. In this work we also explored the relationship between the crystal structure and the electrical properties.

2. Experimental

2.1 *Synthesis of nanosized rare-earth ruthenium pyrochlores*

All the starting chemicals were analytical grade and used directly without further purification. The high purity salts of lanthanum, praseodymium, neodymium, samarium, gadolinium and ruthenium were used as starting materials. The quantities of reactants were calculated according to the stoichiometry in the final product. The precursor of lanthanum–ruthenium tartrate tetrahydrate was prepared by the co-precipitation method by taking $RuCl_3{\cdot}3H_2O$ (4.539 g) and $LaCl_3{\cdot}7H_2O$ (6.448 g) in deionized water (100 ml). The pH of the medium was adjusted to a low enough value (pH $<$ 6), so that hydroxide precipitate does not form. The solution was stirred vigorously with a magnetic stirrer. A disodium tartrate (3%) solution was then added slowly with stirring till a permanent light green tartrate precipitate occurred. Acetone was then added in equal amounts to the precipitate for getting dispersed particles of mixed metal tartrates (which helps enhance the filtration rate). The resultant precipitate of mixed metal tartrate was light green in colour. The solution was filtered after stirring it for 30 min. The precipitate was washed four times with cold distilled water and then with acetone to speed-up the drying. The precipitate was dried at ambient temperature. Similar experimental conditions were used for the preparation of $Ln_2Ru_2(C_4H_4O_6)_6 \cdot nH_2O$, where Ln = Pr^{3+}, Nd^{3+}, Sm^{3+} and Gd^{3+}.

These co-precipitates of rare-earth ruthenium tartrates were decomposed and calcined slowly at 850°C for about 2 h in a platinum crucible under static air atmosphere and then slowly cooled (3°C min^{-1}) down to room temperature. Thus the heat treatment is sufficient for achieving a complete decomposition of tartrate. The powder obtained was polycrystalline. The resulting powders were again ground and calcined at the same temperature for another 2 h. The furnace was turned off and the sample was removed at room temperature. The obtained samples of rare-earth ruthenium perovskite/pyrochlores ($LaRuO_3$, $Pr_2Ru_2O_7$, $Nd_2Ru_2O_7$, $Sm_2Ru_2O_7$ and $Gd_2Ru_2O_7$) were restored in desiccators.

2.2 *Characterization techniques*

The chemical composition of the rare-earth ruthenates was determined using an inductively coupled plasma spectrometer (ICPS) and by chemical analysis. For chemical analysis, recommended procedures were used [17]. The ICPS analysis was performed using a SHIMADZU ICPS-7500 (sequential plasma spectrometer). Duplicate samples were used for this analysis. To avoid errors, a blank solution (distilled water) was run before and after aspiration of every sample into the plasma. A standard solution of each element with maximum concentration (∼100 ppm) was injected into the plasma and the signal intensity was recorded. The same procedure was repeated for remaining known solutions to obtain the calibration curve.

The powder X-ray diffraction (XRD) patterns were recorded from $2\theta = 10°$ to 80° on an X-ray diffractometer model number D8 (Advance BRUCKER AXS). A focusing graphite monochromator equipped after the samples was used for employing Cu Kα radiation ($\lambda = 1.5405$ Å). Rietveld refinement [18] of the X-ray powder data was carried out using GSAS suite of program [19] and EXPGUI graphical interface [20]. The procedures used for the measurements of infrared spectra, apparent density measurement, d.c. electrical conductivity, thermoelectric power and dielectric properties measurements were similar to those reported earlier [21,22]. TEM images were recorded on a JEOL model JEM-1200Ex instrument at acceleration voltage of 100 kV.

Table 1. Observed chemical analysis of rare-earth ruthenates.

	Metal (± 0.5 wt%)											
	Ru		La		Pr		Nd		Sm		Gd	
Compounds	Req.	Found	Req.	Found	Req.	Found	Req.	Found	Req.	Found	Req.	Found
$LaRuO_3$	35.09	34.92 (35.17)*	48.23	48.64 (48.56)*	—	—	—	—	—	—	—	—
$Pr_2Ru_2O_7$	33.95	33.14 (34.21)	—	—	47.28	47.54 (47.18)	—	—	—	—	—	—
$Nd_2Ru_2O_7$	33.54	33.17 (33.43)	—	—	—	—	47.87	48.12 (47.56)	—	—	—	—
$Sm_2Ru_2O_7$	32.87	32.56 (33.10)	—	—	—	—	—	—	48.91	49.10 (48.74)	—	—
$Gd_2Ru_2O_7$	32.15	32.07 (33.96)	—	—	—	—	—	—	—	—	50.02	50.35 (50.32)

* The figures in parenthesis are metal analysis by the inductively coupled plasma (ICP) technique.

3. Result and discussion

3.1 *Solid-state reactivity*

Quantitative tartrate precursors were obtained from saturated metal chloride solution such as $RuCl_3{\cdot}3H_2O$ and rare-earth chlorides with slow addition of 3% sodium tartrate in stoichiometric proportions. The chemical analysis data of rare-earth ruthenium tartrate (i.e., precursors) such as $LaRu(C_4H_4O_6)_3{\cdot}4H_2O$, $Pr_2Ru_2(C_4H_4O_6)_6{\cdot}7H_2O$, $Nd_2Ru_2(C_4H_4O_6)_6{\cdot}8H_2O$, $Sm_2Ru_2(C_4H_4O_6)_6{\cdot}8H_2O$ and $Gd_2Ru_2(C_4H_4O_6)_6{\cdot}7.5H_2O$ are in good agreement with the calculated values (table not shown). The thermal analysis measurements confirmed the presence of the water of hydration of these precursors.

The infrared spectrum showed frequency corresponding to the carboxylate group, hydroxyl group, metal–oxygen, etc. The bidentate linkage of tartrate group with metal was confirmed on the basis of the difference between the antisymmetric and symmetric stretching frequencies. There was no bonding with secondary –OH group (of d-tartaric acid) to metal in solid state [23]. Chain-like polymeric octahedral structures have been assigned to these precursors.

All rare-earth ruthenium tartrates synthesized are paramagnetic at room temperature. These moments are smaller than those obtained by summing up the magnetic moments of the metal ions. This suggests that the metal–metal distance in these systems is large enough to prevent direct orbital overlap. The small depression in the magnetic moment (μ) arises possibly from super-exchange interactions via the carboxylate bridges (i.e., antiferromagnetic interactions).

The thermal decomposition (TGA and DTA) studies of the precursors were used to determine the crystallization temperature of the ruthenates. It shows that all the complexes dehydrate and decompose in the temperature range 30–600°C to produce nearly nanometre-sized ruthenate materials. The infrared spectrum of this residue showed two strong broad bands at ∼594 and ∼412 cm^{-1}. These bands may be tentatively assigned to the rare-earth ruthenium pyrochlore formation. The spectrum further shows a band at ∼2330 cm^{-1}, which indicates the presence of entrapped carbon dioxide on the residue. However, the same residue heated again at 850°C for 2 h and then quenched with air does not show any infrared band at ∼2330 cm^{-1}.

3.2 *XRD studies*

The chemical compositions of rare-earth ruthenates such as $LaRuO_3$, $Pr_2Ru_2O_7$, $Nd_2Ru_2O_7$, $Sm_2Ru_2O_7$ and $Gd_2Ru_2O_7$ samples were determined using an ICPS and by chemical analysis. The observed compositions are summarized in table 1. They are found to be ±0.5% of the nominated values. The results of chemical and ICP analysis showed that all the rare-earth to ruthenium (i.e., Ln:Ru) ratio is 1:1 within the experimental error (<1%) and cations were present in the calcined powders. Therefore, there was no evidence for the loss of ruthenium from particles.

Figure 1 displays the XRD patterns of rare-earth ruthenate samples prepared in this study. In literature [24], the formation of either the perovskite or pyrochlore structure was detected by the appearance of the distinctive strong characteristic XRD lines, especially those corresponding to reflections from the (222) planes in the pyrochlore structure, and from (112) and (200) in the perovskite structure. The XRD patterns of all rare-earth ruthenate samples (figure 1) have indicated the formation of single-phase pyrochlore materials with a face-centred cubic structure except for lanthanum ruthenate, which shows orthorhombic perovskite structure. All the peaks in XRD patterns of ruthenates other than lanthanum ruthenate were indexed successfully in the cubic symmetry (space group Fd-3m) based on the crystal structure of $Ln_2Ru_2O_7$

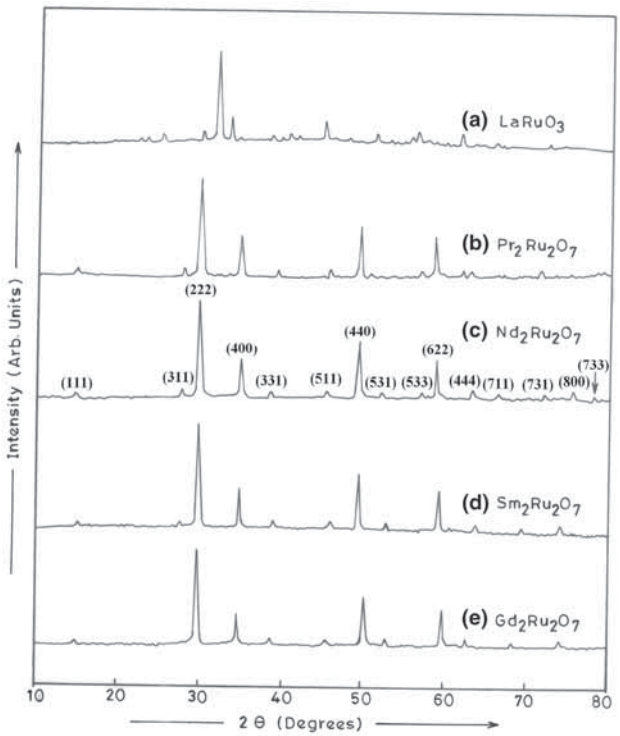

Figure 1. X-ray diffraction patterns of rare-earth ruthenium pyrochlores.

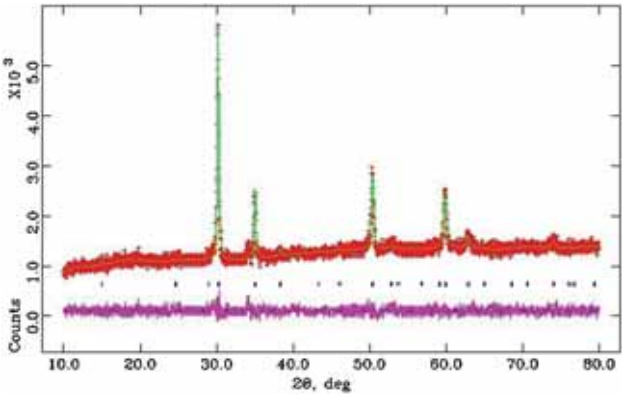

Figure 2. Rietveld plot for $Gd_2Ru_2O_7$ material: observed (red crosses), calculated (green solid line) and difference (lower trace, magenta) PXRD patterns ($x^2 = 3.6$, $R_p = 4.17\%$ and $R_{wp} = 5.26\%$). The tick marks represent the positions of allowed reflections in pyrochlore structure with Fd-3m space group.

Table 2. Rietveld refinement results for $Gd_2Ru_2O_7$.

$Gd_2Ru_2O_7$		
Space group		Fd-3m
R_{wp} (%), R_{F2} (%), χ^2		5.26, 15.6, 3.6
Unit cell composition		$Gd_2Ru_2O_7$
Cell lengths (nm)	a	1.02485(12)
Cell volume (nm^3)	V	107.64(4)
Gd	$x = y = z$	0.5
16	U_{iso}	0.004(2)
Ru	$x = y = z$	0
16	U_{iso}	0.013(6)
O1	X	0.334(6)
48	$y = z$	0.125
	U_{iso}	0.03(3)
O2	$x = y = z$	0.375
16	U_{iso}	0.01(1)

reported earlier by Yamamoto *et al* [25]. The respective *hkl* values are assigned to the peaks in the XRD patterns and their typical values are shown in figure 1 for $Nd_2Ru_2O_7$. As seen from figure 1b–e, the X-ray peaks (111), (331) and (511) indicated single-phase pyrochlore with well-defined superstructure reflection [26], whose intensities depended on the difference in atomic scattering factor between the cations with 3+ and 4+ [27]. Absence of any unindexed line in the XRD patterns indicated that the prepared samples do not contain any impurity phases and are phase-pure pyrochlores of $A_2B_2O_7$ type.

This phase purity of the samples prepared was further authenticated by Rietveld refinement [18] of XRD data. The Rietveld refinement was performed on $Gd_2Ru_2O_7$ XRD data as a representative using the GSAS suite of programs [19] and EXPGUI graphical interface [20]. The initial structural model used for refinement was adapted from the structural data reported by Yamamoto *et al* [25]. The convergence was obtained by simultaneously refining overall scale factor, background, 2θ zero shifts, peak profile, unit cell parameters, thermal displacement parameters and atomic co-ordinates. A Rietveld plot for the powder XRD pattern of $Gd_2Ru_2O_7$ sample is displayed in figure 2, which demonstrates that calculated XRD pattern (green line) based on the pyrochlore structural model refined is in good agreement with the experimentally observed XRD pattern. Thus, the good match of calculated and experimental XRD patterns in the Riteveld plot and absence of any unfitted peak confirm the formation of almost-single-phase $Ln_2Ru_2O_7$ oxides with pyrochlore structures. The crystallographic output of the Rietveld analysis is shown in table 2. The x-parameter of 48f oxygen is 0.334 for the $Gd_2Ru_2O_7$ system and is towards that of the ordered pyrochlore system.

Dickson *et al* [28] reported that the intensities of the (111) reflection is most sensitive to the position of the x-parameter of 48f oxygen. The x-parameter of 48f oxygen changes from 0.313 to 0.375 with increase in disorder in the system and the intensities of characteristic pyrochlore peak approach zero [28]. It is seen from figure 1b–e that the (111) reflection in XRD patterns has very weak intensity relative to stronger reflection (222). This implies that the obtained rare-earth ruthenates have nearly but not completely perfect ordered pyrochlore structure. This indicates the absence of fluorite structure (i.e., disordered) in these ruthenates. Also, the relative radii of the A and B cations are known to influence

the structural disorder on both cation and anion sub-lattices; when $r_A^{3+}/r_B^{4+} > 1.22$ (Ahrens scale) the structure adapted by ruthenates is pyrochlore; otherwise, they adapt a fluorite structure [26]. Ionic radii of cations reported were as follows: for Pr^{3+} 0.116 nm, Nd^{3+} 0.112 nm, Sm^{3+} 0.108 nm, Gd^{3+} 0.106 nm and Ru^{4+} 0.065 nm [29]. As a result, the relative radii of the A and B cations in $Ln_2Ru_2O_7$ (Ln = Pr^{3+}, Nd^{3+}, Sm^{3+} and Gd^{3+}) were between 0.116 and 0.065 nm (thus, $r_A^{3+}/r_B^{4+} > 1.22$), which made all $Ln_2Ru_2O_7$ adapt a stable pyrochlore structure. These results are also consistent with the powder XRD pattern.

The experimentally observed d-spacing values and the relative intensities were compared to those reported in literature [30–32]. The lattice parameter for each compound was then calculated and is shown in table 3. These lattice parameters are close to those reported by the other workers [30–32]. The lattice (cell) parameters obtained using Rietveld analysis for the $Gd_2Ru_2O_7$ system are in good agreement to that calculated manually using '*d*' values of XRD peaks. The relative variation between the observed and calculated lattice constant (spacing) is much lower than 0.2%. These results confirm that the synthesized compound is of single phase as previously described in the literature [33]. The variation of unit cell volume as a function of ionic radii for rare-earth ions is presented in figure 3a. It shows that unit cell volume decreases smoothly with ionic radius of rare-earth ions. It should be noted here that $LaRuO_3$ gets crystallized in the phase other than pyrochlore and hence is not considered while comparing the data in figure 3a.

Wold *et al* [34] have pointed out that in the structure of perovskite, the smaller size of rare-earth ions could not satisfy the tolerance factor requirements for the stability of the perovskite phase. That is, for a given B^{3+} ion size, there is minimum size requirement for the A^{3+} ion, below which no perovskite can form. Since Ru^{3+} is larger, it should be even more difficult to prepare any $LnRuO_3$, where Ln is a rare-earth ion smaller than lanthanum. This is in accord with experimental observations. The perovskite type of other element like Pr, Nd, Sm and Gd could not be formed under the same conditions used for $LaRuO_3$. Instead, the pyrochlores $Ln_2Ru_2O_7$ (Ln = Pr, Nd, Sm and Gd) were major phases. It therefore appears that the phase field defining the perovskite structure for $LaRuO_3$ compounds is shifted further to the left in the lanthanide series so that only La^{3+}, the largest ion, is included. In this connection, it may also be noted that no $La_2Ru_2O_7$ pyrochlore exists.

3.3 *Particulate properties*

The particulate properties like density, porosity and average crystallite size of rare-earth ruthenium pyrochlores are summarized in table 3. It is noticed that the X-ray densities, D_X of rare-earth ruthenates, increase with the ionic radius of rare-earth ions (figure 3b). The X-ray densities (D_X) are higher than the apparent density (D). This is attributed to the existence of pores. The porosity (P) and apparent density (D) for

Table 3. X-ray powder diffraction data, particulate properties and infrared spectral data of rare-earth ruthenates.

Compounds	Lattice parameter '*a*' (nm)	Unit cell volume $(nm)^3$	Mean crystallite size $\langle D\rangle_{X\text{-ray}}$ (nm) ± 10%	X-ray density D_X (g cm^{-3})	Apparent density D (g cm^{-3})	Porosity $P = 1 - D/D_X$	Average particle size (from TEM) (nm)	Infrared spectral bands (cm^{-1})	
								υ_1	υ_2
$LaRuO_3$	$a = 0.552$ $b = 0.582$ $c = 0.781$	0.251	35.92	7.622	2.218	0.709	73.8	588, 444	403
$Pr_2Ru_2O_7$	1.039	1.121	31.38	7.057	2.437	0.654	58.6	594, 482	390
$Nd_2Ru_2O_7$	1.036	1.111	29.12	7.198	2.554	0.645	52.7	613, 492	401
$Sm_2Ru_2O_7$	1.030	1.092	28.74	7.473	2.826	0.621	36.4	619, 500	407
$Gd_2Ru_2O_7$	1.025	1.076	27.92	7.754	2.962	0.618	45.3	658, 511	413

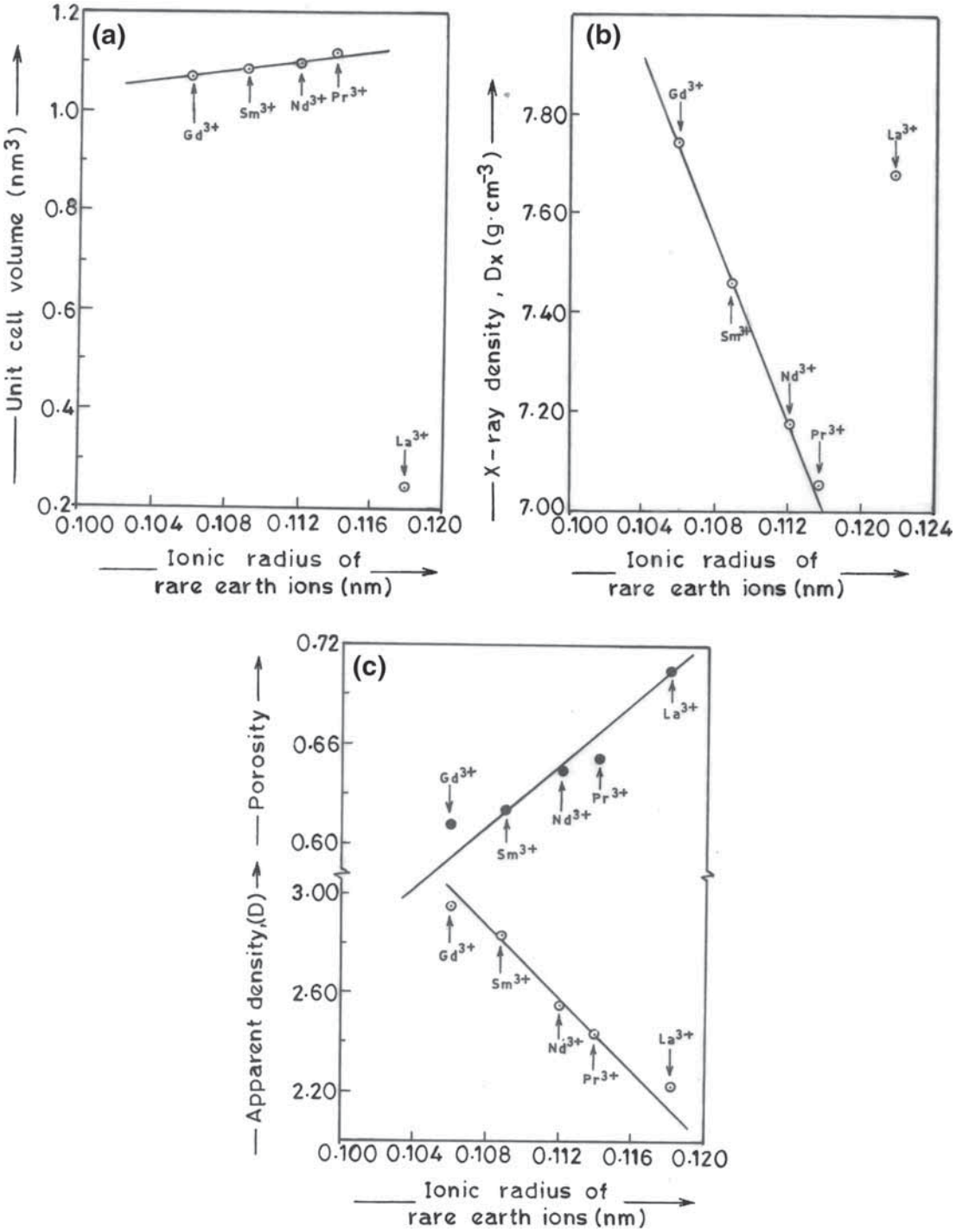

Figure 3. (**a**) Unit cell volume as a function of ionic radius of rare-earth ions. (**b**) X-ray density (D_X) as a function of ionic radius of rare-earth ions. (**c**) Porosity (P) and apparent density (D) as a function of ionic radius of rare-earth ions.

these rare-earth ruthenates are illustrated in figure 3c. This figure shows that the higher porosity corresponds to lower apparent density. These results are explained on the basis that La^{3+} has bigger ionic radius than Gd^{3+} in the series.

The crystallite size $\langle D \rangle_{X\text{-ray}}$ calculated for all rare-earth ruthenates was based on the FWHM values (after correction for instrumental broadening effect) extracted from peak fitting software and also crystallite size from XRD peak-width at half-maximum of three successive diffraction peaks using the Debye–Scherrer equation [35]. We believe that these values are almost similar to that obtained after Rietveld fitting and hence we have decided to continue with

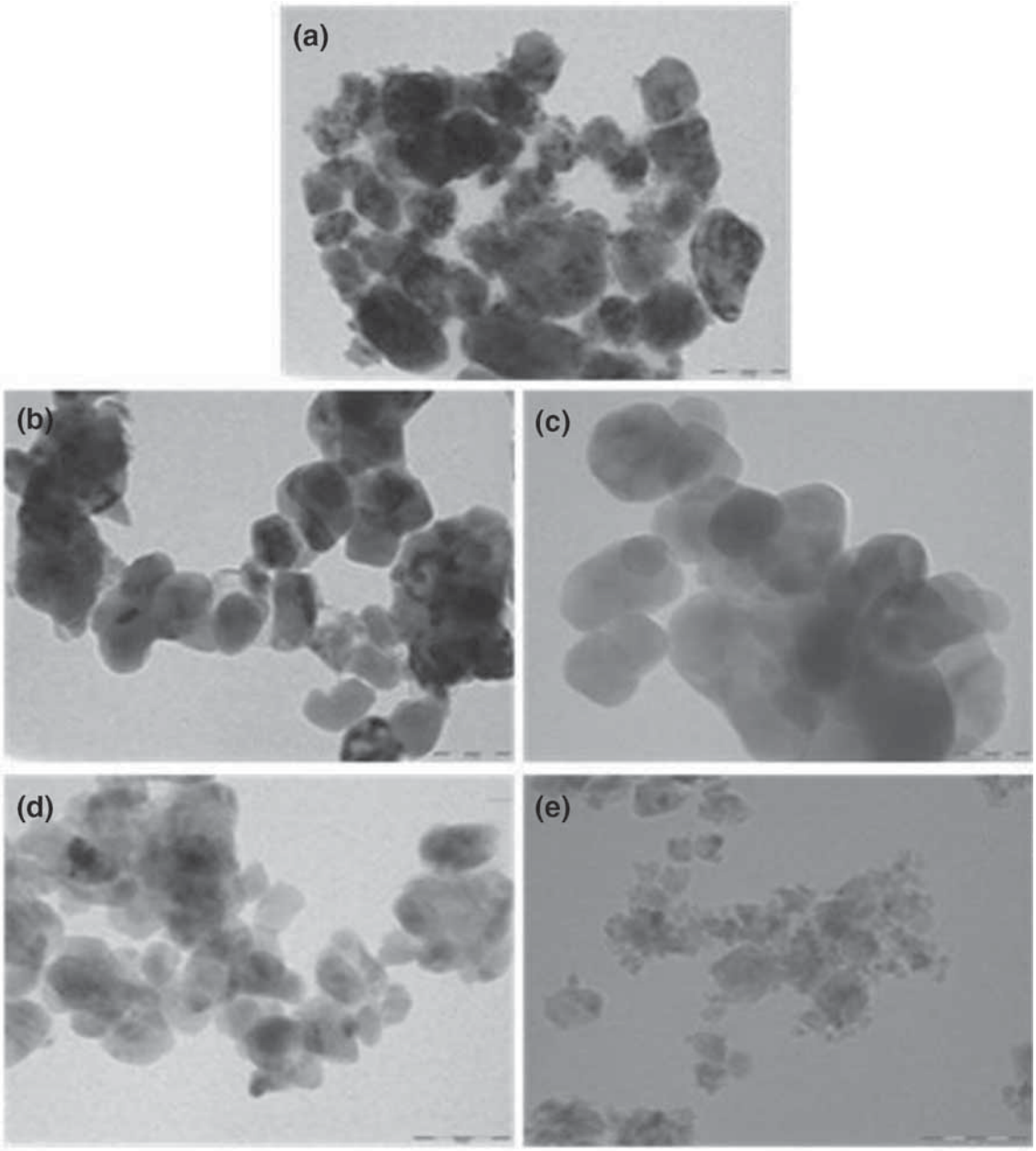

Figure 4. TEM micrographs of rare-earth ruthenates: (**a**) $LaRuO_3$, (**b**) $Pr_2Ru_2O_7$, (**c**) $Nd_2Ru_2O_7$, (**d**) $Sm_2Ru_2O_7$ and (**e**) $Gd_2Ru_2O_7$.

crystallite size values obtained by the traditional peak fitting method. The observed crystallite sizes $\langle D \rangle_{\text{X-ray}}$ obtained from the Debye–Scherrer equation are given in table 3. It is seen from this table that the mean crystallite size for all ruthenates is in the range of 27.92–35.92 nm.

The TEM micrograph of rare-earth ruthenium pyrochlore (figure 4) revealed that the particles were plate-like, non-aggregated and dense; and some of the platelets have already been destroyed. The TEM results of rare-earth ruthenate indicated that the nanocrystals were polycrystalline with good dispersibility. The average particle sizes of these samples were found to be less than 73.8 nm, as shown in table 3. This figure confirms the formation of nano-particles of rare-earth ruthenates.

3.4 *Infrared spectral studies*

Infrared spectral frequencies of rare-earth ruthenates, i.e., $LaRuO_3$, $Pr_2Ru_2O_7$, $Nd_2Ru_2O_7$, $Sm_2Ru_2O_7$ and $Gd_2Ru_2O_7$, are shown in table 3. All the ruthenates show strong

absorption band over 584–658 and 413–511 cm^{-1} (ν_1) and 390–413 cm^{-1} (ν_2), which are characteristics of pyrochlore structure [36,37]. The absorption bands at (ν_1) belong to stretching vibrations of Ru–O bridge; the absorption bands (ν_2) belong to deformed vibrations of O–Ru–O bridge [38]. It is noticed from table 3 that, on replacing La^{3+} with heavier rare-earth like Pr^{3+}, Nd^{3+}, Sm^{3+} and Gd^{3+}, the ν_1 and ν_2 shift to progressively higher wavenumbers, because the ionic radius of La^{3+} (0.118 nm) is larger than that of Gd^{3+} (0.106 nm). This would suggest that the La^{3+} and Ru^{4+} ions are sufficiently heavy to form a quasi-stationary internal frame, while the oxygen ions move in the potential wells formed by the metal ions. Since the charge distribution in the well (and hence the vibrational force constant) depends on the effective inter-atomic distance, which varies with rare-earth ions, the peak frequencies appear (ν_1 or ν_2) to depend on the ionic radius of the rare earth rather than on the atomic mass.

3.5 *Electrical conductivity studies*

Figure 5 illustrates the dependence of electrical conductivity (σ) against reciprocal temperature for the pyrochlore rare-earth ruthenates, i.e., $LaRuO_3$, $Pr_2Ru_2O_7$, $Nd_2Ru_2O_7$, $Sm_2Ru_2O_7$ and $Gd_2Ru_2O_7$. It shows the initial decrease in electrical conductivity (σ) in the temperature range of 301–350 K, which corresponds to desorption of absorbed water molecules on the particle surface. The conductivity (σ) then increases linearly with increasing temperature. The activation energy E_a (eV) calculated from the slope of the lines is listed in table 4. It is observed that the activation energy for all samples is in the range of 0.217–0.431 eV, which exhibits semi-conducting behaviour. This probably corresponds to oxygen non-stoichiometry and the valence stabilities of ruthenium being able to change its valence fare more easily i.e. valence charge of Ru^{4+} because of stable rare-earth element.

The electrical data plotted in figure 5 show a fairly high conductivity of approximately 7.58×10^{-8} to $8.91 \times 10^{-6}\ \Omega^{-1}\ cm^{-1}$ for both perovskite $LaRuO_3$ and pyrochlore $Ln_2Ru_2O_7$ (Ln = Pr, Nd, Sm and Gd). The positive temperature dependence is characteristic of metallic/semi-conducting materials, but relatively high resistivity suggests that these oxides are poor 'metals'. It is fair to assume that the resistivity of single crystals would be considerably lower.

In perovskite $LaRuO_3$, La^{3+} has larger size and at the same time, Ru^{3+} is less strongly bonded because of its larger size and smaller charge. The bridging angles for the corner-sharing RuO_6 octahedra linked into the zig-zag chains play an important role in super-exchange interaction and the formation of electrical conduction bonds for perovskite-type $LaRuO_3$ compound. The effects are additive, both leading to a decreasing Ru–O interaction, and presumably a borrower π^*-bond. In $LaRuO_3$, the bandwidth has been sufficiently decreased so that anti-ferromagnetic behaviour is observed, which appears to be more characteristic of narrow bands [39].

From qualitative band-model consideration of the type discussed by Goodenough [40], $LaRuO_3$ has two types of

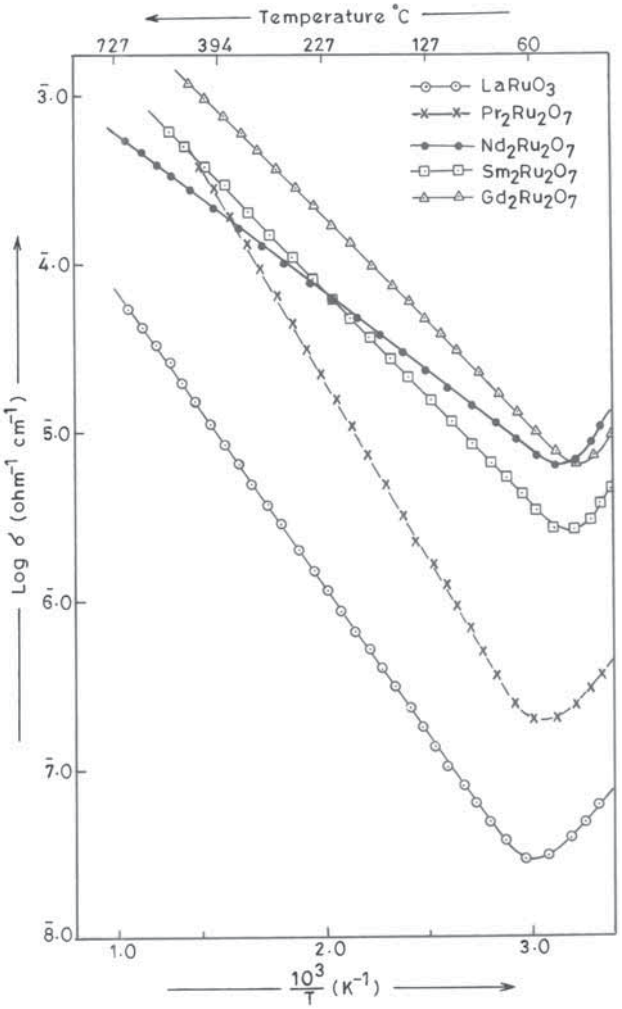

Figure 5. Plot of log σ against T^{-1} of rare-earth ruthenium pyrochlores.

interactions. The first involves t_2g orbitals on Ru and $p(\pi)$ orbitals on the O atoms and is $Ru-O\pi$ interaction. The second involves $p(\sigma)$ orbitals on Ln (i.e., rare earth) and the same set of O atoms. This results in a set of partially occupied $Ru-O\pi^*$ levels, which lie just below an empty $Ln-O\sigma^*$ band. Thus, $LaRuO_3$ should be metallic with a $5/6(d^5)$ filled π^*-band formed from $(Ru)t_{2g}-(O)_p\pi$ covalent interactions. The electrical conduction would then become an activated process, via transfer of the electrons from $t_{2g}(\pi^*)$ to e.g., σ^* levels, which would presumably also exist as band states, σ bonding being stronger than π bonding.

The cubic pyrochlore structure adapted by ternary ruthenates ($Ln_2Ru_2O_7$) is based on a framework of corner-sharing RuO_6 octahedrons that are linked into the zig-zag chains, with the Ru–O–Ru angle of around 135°, while for perovskite structure the Ru–O–Ru angle is 180°. The octahedral ligand field experienced by the Ru^{4+} ions splits the 4d sub-shells into more stable t_{2g} and less stable e_g components. Each oxygen atom is fourfold coordinated to two ruthenium atoms and

Table 4. Electrical conductivity and dielectric properties of rare-earth ruthenates.

Compounds	Temperature corresponding to desorption of adsorbed water (K)	Activation energy E_a (eV)	Thermoelectric power measurements (charge carriers)	Room temperature dielectric constant (ε') at 1 kHz
$LaRuO_3$	342	0.345	n type	82.07
$Pr_2Ru_2O_7$	335	0.431	n type	65.26
$Nd_2Ru_2O_7$	319	0.217	n type	96.23
$Sm_2Ru_2O_7$	322	0.260	n type	60.31
$Gd_2Ru_2O_7$	325	0.287	n type	61.08

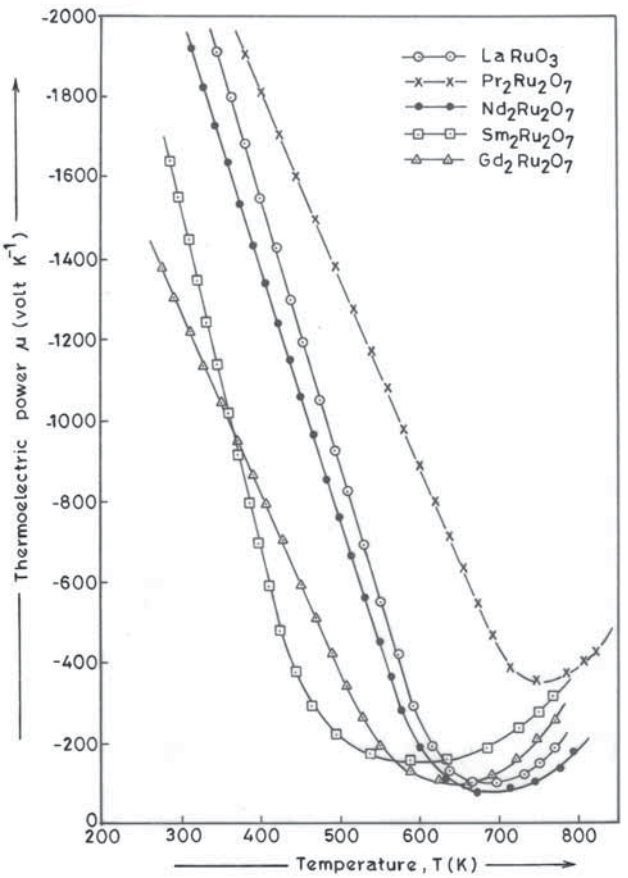

Figure 6. Plot of thermoelectric power μ (V K^{-1}) against temperature T (K) of rare-earth ruthenium pyrochlores.

two rare-earth atoms. The Ru:4d (t_{29}) orbitals of neighbouring Ru atoms can have π-type orbital interaction through the Ru–O–Ru bridges [41]. These interactions are enhanced by a decrease in the Ru–O–Ru angle and a lengthening of the Ru$-$Oπ, thereby decreasing overall width of t_{2g}-block bands.

It is expected that there will be an 'inductive' effect, where Ru^{3+} ion competes with the Ru^{4+} ion and withdraws electron density from the Ru-Oπ bonding network. The magnitude of the inductive effect increases as the size of the Ln^{3+} ion decreases, leading to more semiconducting character for smaller Ln^{3+} pyrochlore. Thus the electrical properties change is related to their structural changes such as (i) the increase in the Ru–O bond length in the RuO_6 octahedron, (ii) the reduction of the O–Ru-O angle and the distortion of RuO_6 octahedron reducing the Ru–O overlap integrals, (iii) the increase in the bending of the RuO_6 zig-zag chains and (iv) the strength of the R$-$O$_\sigma$ interaction increasing the acidic character with decreasing size of the rare-earth atoms.

3.6 *Thermoelectric power measurements*

Figure 6 shows the temperature variation of the thermoelectric power (μ) for the rare-earth ruthenium pyrochlores. The sign of thermoelectric power was negative for all samples over the whole temperature range, which indicates n-type semiconductivity as expected. The high temperature measurements of the thermoelectric properties indicate that rare-earth ruthenate pyrochlore compound has excessively high electrical resistivity for it to be a useful thermoelectric material.

All ruthenates show a very steep decrease of the thermoelectric power from room temperature to around 680 K and then slightly increases up to 800 K. This may happen only when charge carriers are localized on the defect centres, which are inherently present in the solids. Obviously carriers are trapped by the Ru^{4+} ion. The band structure of rare-earth ruthenates has narrow Ru:4d (t_{2g}) band at Fermi energy, E_F, which enhances the electron–electron interaction. Despite this the rare-earth ions (Ln^{3+}) do not participate directly in the conduction process. Therefore, we believe that the major carriers in these compounds are electrons.

3.7 *Dielectric studies*

The room temperature dielectric constants of rare-earth ruthenium pyrochlores are given in table 4. The dielectric constant (ε') against temperature and frequency of $LaRuO_3$, $Pr_2Ru_2O_7$, $Nd_2Ru_2O_7$, $Sm_2Ru_2O_7$ and $Gd_2Ru_2O_7$ is plotted in figure 7a and b, respectively.

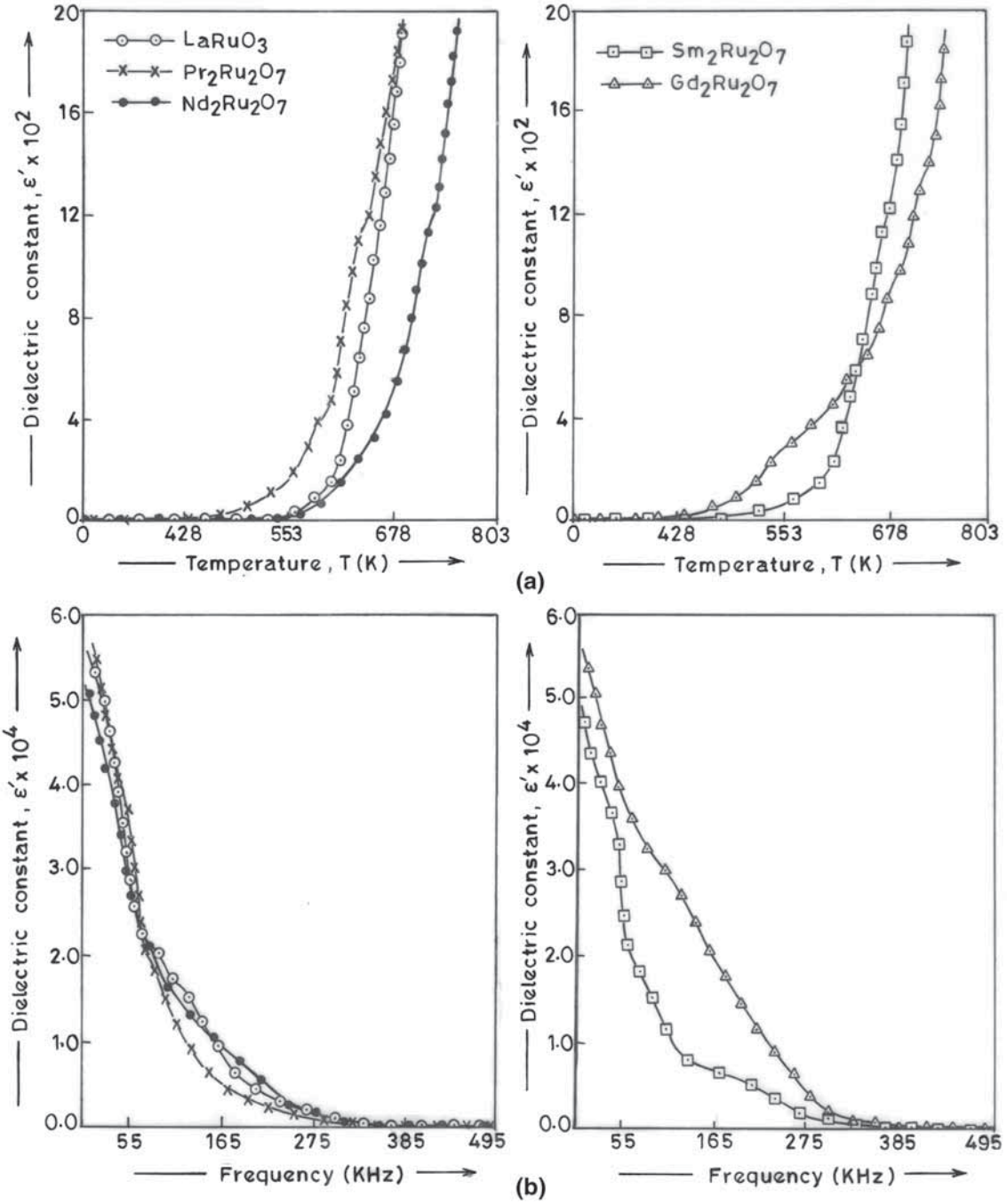

Figure 7. (**a**) Variation of dielectric constant (ε') with temperature for rare-earth ruthenium pyrochlores. (**b**) Variation of dielectric constant (ε') with frequency for rare-earth ruthenium pyrochlores.

In the pyrochlore ($Ln_2Ru_2O_7$) structure, however, there are a number of possibilities. The cooperative hopping of the loosely bound 'seventh' oxygen ion in the pyrochlore structure [42] has been proposed as the origin of ferroelectricity in $Cd_2Nb_2O_7$, and it is possible that this mechanism may be involved in the behaviour of the rare-earth ruthenium pyrochlores. In addition, vacancies in the pyrochlore structure are believed to have a significant role as found in the perovskite $LaRuO_3$.

Returning to the data of figure 7a, above ~500 K, an enormous increase in dielectric constant for all compounds is observed. The dielectric behaviour of ruthenate indicates that the mechanism of dielectric polarization is similar to that of the conduction process. It is observed that the electron exchange interaction between Ru^{3+} and Ru^{4+} ions results in the local displacement of the electron in the direction of applied field, which determines the polarization of the ruthenates. According to Koops [43], the dielectric constant

is inversely proportional to the square root of resistivity. Therefore, the increase in dielectric constant with temperature is expected.

Figure 7b shows the variation of dielectric constant (ε') with frequency in the range 1–500 kHz for rare-earth ruthenates. The variation of dielectric constant with frequency reveals (figure 7b) the dispersion due to Maxwell–Wagner [44,45]-type interfacial polarizations. According to the Maxwell–Wagner model, the dielectric structure of a rare-earth ruthenate material is assumed to be made up of two layers, first layer being a conducting layer consisting of large ruthenate grains and other being the grains boundaries that are poor conductors.

4. Conclusions

A series of nano-sized rare-earth ruthenates $Ln_2Ru_2O_7$ (Ln = La^{3+}, Pr^{3+}, Nd^{3+}, Sm^{3+} and Gd^{3+}) were successfully synthesized by thermal decomposition of the mixed-metal tartrate precursors at 850°C. The XRD patterns for the rare-earth ruthenates indicated the formation of single-phase pyrochlore with a cubic structure except lanthanum ruthenate, which shows perovskite orthorhombic structure. The unit cell volume decreases smoothly with ionic radius of the rare-earth ions. TEM micrographs of rare-earth ruthenium pyrochlores show that the average particle size is in the 36.3–73.8 nm range. All rare-earth ruthenates are semiconductors and major carriers are electrons. The conduction mechanism of these compounds seems to be oxygen non-stoichiometry. The thermoelectric power for rare-earth ruthenates showed n-type semiconductivity throughout the temperature range. The carriers are trapped by the Ru^{4+} ions. The dielectric constant against temperature and frequency for these ruthenates showed the dispersion due to Maxwell–Wagner-type interfacial polarization.

References

[1] Aschcroft A T, Cheetham A K, Foord J S, Green M L, Grey C P, Murrell A J *et al* 1990 *Nature* **344** 319
[2] Egdell R G, Goodenough J B, Hamnett A and Naish C C 1983 *J. Chem. Soc. Faraday Trans. I* **79** 893
[3] Carcia P F, Ferreti A and Suna A 1982 *J. Appl. Phys.* **53** 5282
[4] Bouchard R J and Gillson J L 1971 *Mater. Res. Bull.* **6** 669
[5] Longo J M, Raccah P M and Goodenough J B 1969 *Mater. Res. Bull.* **4** 191
[6] Che M and Bennet C O 1989 *Adv. Catal.* **36** 55
[7] Subramanian M A, Aravamudan G and Subba Rao G V 1983 Prog. *Solid State Chem.* **15** 55
[8] Wuensch B J and Eberman K W 2000 *J. Miner.* **52** 19
[9] Mandal G P, Garg N, Sharma S M and Tyagi A K 2006 *J. Solid State Chem.* **179** 1990
[10] Mandal G P, Deshpande S K and Tyagi A K 2008 *J. Mater. Res.* **23** 911
[11] Mandal G P, Krishna P S R and Tyagi A K 2010 *J. Solid State Chem.* **183** 41
[12] Kafalas J A and Longo J M 1970 *Mater. Res. Bull.* **5** 193
[13] Kanno R, Takeda Y, Yamamoto T, Kawamoto Y and Yamamoto O 1993 *J. Solid State Chem.* **102** 106
[14] Darton R J, Turner S S, Slaon J, Lees M R and Walton R I 2010 *Cryst. Growth Des.* **10** 3819
[15] Senzaki Y, Hampden-Smith M J, Kodas T T and Hussler J W 1995 *J. Am. Ceram. Soc.* **78** 2977
[16] Abate C, Esposito V, Duncan K, Nino J C, Gattia D M, Achsman E D *et al* 2010 *J. Am. Ceram. Soc.* **93** 1970
[17] Vogel A I 1968 *Quantitative inorganic analysis* Japan: The English Language Soc.
[18] Rietveld H M 1967 *Acta Crystallogr.* **22** 151
[19] Larson A C and von Dreele R B 1994 *Generalized structure analysis system (GSAS)* LAUR 86-748. Los Alamos, New Mexico: Los Alamos National Laboratory
[20] Toby B 2001 *J. Appl. Crystallogr.* **34** 210
[21] Nikumbh A K, Phadake M M and Latkar A A 1994 *J. Magn. Magn. Mater.* **131** 189
[22] Nikumbh A K, Pawar R A, Nighot D V, Gugale G S, Sangale M D, Khanwilkar M B *et al* 2014 *J. Magn. Magn. Mater.* **355** 201
[23] Nakamoto K 1970 *Infrared spectra of inorganic and coordinated compounds* 2nd edn. (New York: Wiley-Interscience)
[24] Greatex R, Hu G and Munro D C 1986 *Mater. Res. Bull.* **21** 797
[25] Yamamoto T, Kanno R, Takeda Y, Yamamoto O, Kawamoto Y and Takano M 1994 *J. Solid State Chem.* **109** 372
[26] Govindan K V, Kutty S J, Mathews C K, Rao T N and Varadaraju U V 1995 *Solid State Ion.* **80** 99
[27] Izu N, Omatta T and Otsuk-Yao-Matsuo S 1998 *J. Alloys Compd.* **270** 107
[28] Dickson S J, Hawkings K D and White T J 1986 *J. Solid State Chem.* **82** 146
[29] Mogensen M, Sammes N M and Tompsett G A 2000 *Solid State Ion.* **129** 63
[30] ASTM File Number 25-426
[31] Kennedy B J 1995 *Acta Crytallogr.* **51** 790
[32] Taira N, Wakeshima M and Hinatsu Y 1999 *J. Phys.: Condens. Matter* **11** 6983
[33] Douma M, Chtoun E H, Trijillano R, Rives V and Khayroun S 2009 *Ann. Chim. Sci. Mater.* **34** 21
[34] Wold A, Arnott R J and Croft W J 1963 *Inorg. Chem.* **2** 972
[35] Klug H P and Alexander A E 1954 *X-ray diffraction procedure* (New York: Wiley Inter-science) Chapter 9
[36] Subramanian M A, Aravamudan G and Subbarao G V 1983 *Prog. Solid State Chem.* **15** 78
[37] Gong X, Wu P, Chen W and Yang H 1998 *J. Mater. Res.* **13** 469
[38] Banerjee A, Mishra R and Singh Z 2001 *Solid State Ion.* **201** 42
[39] Longo J M, Raccah P M and Goodenough J B 1968 *J. Appl. Phys.* **39** 132
[40] Goodenough J B 1965 *Bull. Soc. Chim. Fr.* **4** 1200
[41] Cox P A, Goodenough J B, Tavener P J, Telles D and Egdell R G 1986 *J. Solid State Chem.* **62** 360
[42] Viehland D, Jang S J, Cross L E and Wutting M 1990 *J. Appl. Phys.* **68** 2916
[43] Koops C G 1951 *Phys. Rev.* **83** 121
[44] Maxwell J C 1973 *Electricity and magnetism* vol I (New York: Oxford University Press) p 828
[45] Wagner K W 1973 *Am. Phys.* **40** 817